



Enhancement of Corrosion Resistance and Tribological Properties of LA43M Mg Alloy by Cold-Sprayed Aluminum Coatings Reinforced with Alumina and Carbon Nanotubes

Usman Ahmed^{1,2} · Lui Yi¹ · Lu Fei Fei¹ · Muhammad Yasir² · Chang-Jiu Li¹ · Cheng-Xin Li¹

Submitted: 5 July 2020 / in revised form: 3 December 2020 / Accepted: 4 December 2020 / Published online: 20 January 2021
© ASM International 2021

Abstract Magnesium is a suitable material for structural and aerospace applications owing to its high strength to weight ratio, yet the wide usage of Mg alloys is restricted due to their poor corrosion and mechanical properties. In this study, cold gas spraying method was used to produce pure Al, Al-Al₂O₃ and Al-Al₂O₃-CNTs coatings with feedstock powder containing Al admixed with 5 wt.% Al₂O₃ and 1 wt.% CNTs to improve electrochemical and tribological properties of Mg-LA43M alloy. X-ray diffraction spectroscopy and scanning electron microscopy were performed for compositional and microstructural analysis of feedstock powders as well as coatings. Furthermore, corrosion properties of coatings were examined by photodynamic polarization, electrochemical spectroscopy and long-term immersion test in 3.5% NaCl solution. The obtained results were correlated with microstructural analysis and we found that reinforcement of hard particles, especially CNTs, resulted in better corrosion resistance of MMC coatings as compared to Mg substrate and pure Al coatings. Reinforcements of Al₂O₃ and CNTs also improved the sliding wear resistance of the coatings. Al-Al₂O₃-CNTs exhibited lower coefficient of friction and wear rate than the Mg substrate, pure Al, and Al-Al₂O₃ coatings due to the denser microstructure.

Keywords aluminum matrix coatings · cold spray process · carbon nanotubes · corrosion resistance

Introduction

Owing to their lightweight characteristics, magnesium and its alloys can replace traditional metals (Ref 1). Simultaneously, magnesium has high damping and specific strength with excellent electromagnetic shielding ability (Ref 2, 3), but wide range use of Magnesium and its alloys in aerospace and automotive industry is limited due to its inferior corrosion and mechanical properties. The corrosion of magnesium-lithium alloys is spontaneous, highly prone to occur and is irreversible due to their high chemical activity (Ref 4). There are numerous surface engineering techniques to modify and improve the surface properties of magnesium alloys (Ref 5), but these existing surface modification techniques have restricted performance due to certain limitations such as cost. While several thermal spray techniques have economic advantages in coating magnesium alloys, porosity in these coatings requires several post coating handling or treatment processes in order to yield dense coatings that have suitable corrosion and wear resistance (Ref 6-8).

Cold spraying technology is a relatively new and environmentally friendly technology among the surface treatment methods, in which compressed gas is used to accelerate the micron-sized particles to supersonic velocities (up to 500-1000 m/s) and deposit on the substrate to form protective coatings (Ref 9). The flowing carrier gas has very large pressure difference (up to 3.5 MPa) (Ref 10). Cold spray possesses outstanding advantages such as preparation of dense coatings, negligible effect on substrate during coatings, and material being sprayed having

✉ Cheng-Xin Li
licx@mail.xjtu.edu.cn

¹ State Key Laboratory for Mechanical Behavior of Materials, School of Materials Science and Engineering, Xi'an Jiaotong University, Xi'an, Shaanxi, China

² Department of Materials Science and Engineering, Institute of Space and Technology, Islamabad 44000, Pakistan

minimum effects like oxidation, phases change, etc. (Ref 11). Cold spraying has been used to deposit many types of materials including pure metals (Ref 12) alloys (Ref 13) and composite materials (Ref 14). For the purpose of producing protective coatings on Mg alloy, aluminum powder is the most desirable of all powders used for cold spraying due to its low density and to the standard electrode potential of aluminum being closer to that of magnesium alloys than other metals. Also aluminum has the lowest galvanic corrosion tendency when in contact with Mg alloys (Ref 15). However, due to low density and high specific heat of aluminum, imperfect flattening of particles upon impact takes place and it results in formation of pores. Low density means lower kinetic energy of the sprayed particles. Further, high specific heat (i.e., high amount of heat needed to increase the temperature of a unit mass by 1 K) means that plastic dissipation upon impact might not succeed to increase the temperature of an impacting particle up to the required threshold for adiabatic shear instability. Porosity has detrimental effect on mechanical properties of coatings such as hardness, wear and corrosion resistance (Ref 16). So, it is essential to suppress the pores formation during coating deposition in order to produce coatings with better mechanical properties (Ref 17). The mechanical properties of cold-sprayed aluminum coatings can be improved by incorporating it with hard phase cermet or ceramic reinforcing particles to produce metal matrix composite coatings (Ref 18). Many researchers have found out that alumina (Al_2O_3) blended with aluminum powder results in coatings with better mechanical properties (Ref 19, 20). But the final content of alumina in produced coatings must be limited to 20 wt.% as waste of powder becomes an issue when used on an industrial scale (Ref 11). The use of hard ceramic phases such as alumina as reinforcement improves the densification of the microstructure of coatings by decreasing the porosity up to 2–8% and by improving the bonding between substrate and coating (Ref 11). Other studies have expanded the production of MMC cold-sprayed coatings to use nanofillers as reinforcements in order to obtain coatings with better properties (Ref 21). Since carbon nanotubes (CNTs) have been discovered many researchers have devoted their interest to use them as reinforcing material in metal matrix composites MMCs (Ref 22) owing to the fact that CNTs have good mechanical properties such as stiffness up to 1TPa and strength of 63 GPa. Aluminum matrix composites reinforced with multi-walled carbon nanotubes (MWCNTs) are promising materials for applications in various high-tech industries (Ref 23).

This work explores the usage of cold spray technologies for manufacturing of hard phase hardened aluminum coatings. Aluminum coatings with two types of reinforcing particles, namely Al_2O_3 and CNT particles are analyzed in

this research. Homogenous mixing of CNTs and Al_2O_3 powder particles with aluminum is necessary for better mechanical and corrosion properties. The goal of reinforcing CNTs in metal composite is to manufacture coatings with improved corrosion and tribological properties than pure aluminum coatings. CNTs have very low size, thickness, large specific surface area and are vulnerable to entanglement, so a reasonable amount of CNTs will boost the properties of the metal composite. CNTs with outstanding mechanical properties resist the externally imposed strain on the metal matrix and thereby strengthen its wear properties. Through reinforcing the CNTs, owing to the difference between the properties of the metallic framework and the CNTs, the density of the material dislocations increases and the strengthening of the dislocations happens. Also, CNTs play an important part in grain refining of MMCs, the heavy pinning impact of CNTs on grain boundary effectively inhibits grain development and was found to be the key explanation behind grain refining in MMCs. CNTs also exert a bridging role between the surface layer of corrosion product and the underlying metallic surface that increases the resistance to corrosion (Ref 24). As mentioned before, our purpose is to prepare aluminum composite coatings with Al_2O_3 + CNTs as reinforcement. The basic purpose of this is to prepare coatings with dense microstructure with very few micropores to enhance the electrochemical and tribological behavior of Mg substrate.

Experimental

Feedstock Powder

Feedstock powders for deposition of coatings were prepared at the thermal spray laboratory of Xian Jiaotong University. The powders used to prepare coatings were commercially available pure aluminum powder with particles size of ~ 20 – 25 micrometers and spherical morphology. Aluminum powder was reinforced with 5 wt.% alumina Al_2O_3 and with 5 wt.% Al_2O_3 + 1 wt.% CNTs, respectively. Reinforced powders were prepared via high energy ball milling (at the thermal spray laboratory of Xian Jiaotong University). Uniform distribution of reinforcing particles potentially results in better mechanical properties of the composites (Ref 26). Therefore, careful synthesis parameters are required during ball milling to restrain the clustering of particles. To prevent unadorned cold welding of powders, 0.25 wt.% stearic acid was added to the powder mixture in the ball mill. 10 mm stainless steel balls are also added and ball to powder weight ratio was 10:1, the speed of milling was maintained at 30 RPM. Ball milling was done for 12 h with rest period of 1 min and

running period of 1 min in order to prevent the overheating of powder mixture. Argon gas was purged into the vessels containing the ball milling mixture in order to remove air and to prevent formation of any intermetallic during milling. The morphology of reinforced powders after ball milling was not as spherical as pure aluminum this is due to the deformation of powders during ball milling.

Coating Deposition

In this study, the coatings were prepared by cold spray equipment DWCS-2000 (Dewie automation company Xian, China) with an optimized de Laval nozzle (Ref 25). Convergent and divergent nozzle design was used in this system, feedstock powder was fed along the axis. The diameter of throat, diameter of outlet and length of divergent nozzle were 2.72, 6.1 and 150 mm, respectively. Powder feeder rate was kept at 25 g/min. The powder feeder used has maximum pressure limit of 4 MPa. Nitrogen gas is used as both main gas and powder feeder carrier gas and its stagnation pressure was kept at 3 MPa for main gas and 3.2 MPa for carrier gas. The pressure of the powder carrier gas was higher than that of main gas in order to ease powder injection into the jet. The substrate was fixed to stationary sample holder while the nozzle was attached with an automated robotic arm capable of computer-controlled three-dimensional motion to ensure better deposition of coatings. Standoff distance between nozzle and substrate was 20 mm, and nozzle transverse speed was 40 mm/s. The substrate used was LA43M magnesium which was sandblasted with alumina grit under a compressed air pressure of 0.6 MPa prior to coating deposition in order to enhance the adhesion of coating with substrate. Detailed schematic representation of cold spray process is presented in Fig. 1.

Characterization

The external morphology of powders was examined by field emission scanning electron microscope SEM. The powders were speckled on adhesive carbon tape and examined by secondary mode of FESM (MIRA3 TESCAN). Particle sizes of feedstock powders were measured by laser particle size analyzer (MALVERN 3000). X-ray diffractometer (XRD) operated at 35 kV and 25 mA was used to characterize the phases present in feedstock powders. The cross section of all coatings was polished according to metallographic standards and examined by FESEM also. Micro-Vickers hardness test was performed to determine the hardness of coatings. The load was 25 g, and the indenter time was 15 s. Three values of micro-hardness are taken at each point and their average is

presented. The corrosion resistance of coatings was inspected by open circuit potential (OCP), electrochemical impedance spectroscopy (EIS) and potentiodynamic polarization (PDP). The tests were performed in 3.5 wt.% NaCl solution using a conventional three electrode cell by an electrochemical workstation (Prostat). The electrodes used were saturated calomel electrode (SCE) as reference, Graphite as standard electrode and our test sample cut in area around 1.2 cm² as working electrode. All the samples were ground to 1200 grit before tests for stable results. The OCP test was performed firstly in 3.5 wt.% NaCl solution, and then the PDP test is conducted after 2 h, so that by the beginning of PDP test the OCP value had become stable. The PDP measurement was performed at a sweep rate of 1 mV/s, and the over-potential range for PDP test was ± 0.25 V. The corrosion potential and corrosion current density were obtained from the polarization curves by Tafel-type fitting using software in the instrument. For EIS measurement, the frequency ranged from 10 kHz to 0.01 Hz (ten points per decade) and the AC amplitude was 10 mV around the OCP. The EIS spectra results were analyzed using ZSimpWin 3.10 software and fitted by equivalent circuit models. All the samples were also ground to 1200 grit before wear tests. The wear test was performed on a Pin on disk tribometer (MT/60/NI/Ht/L MICROTTEST S.A.) with 3 mm stainless steel (AISI 420) ball as counter body to slide against samples. The wear test was performed on ASTM G99 standard. While test conditions were: $F = 3$ N; $v = 0.1$ ms⁻¹, $T = 23$ °C; relative humidity range 12 to 78%; laboratory air. During the wear test, the disk was rotated at a speed of 400 rpm for a total of 5000 revolutions. The wear mass loss of specimens was measured using an electric balance with a sensitivity of 10⁻⁴ g. For each electrochemical and wear test, three samples were prepared and average values of end results are presented in this study.

Result and Discussion

Microstructural Investigation

The purpose of this investigation was to ensure the homogeneous distribution of CNTs and Al₂O₃ particles with Al powder. Scanning electron micrograph results of as received aluminum powder, alumina reinforced aluminum powder (Al + Al₂O₃) and Carbon Nanotubes + Alumina reinforced aluminum powders (Al + Al₂O₃ + CNTs) after ball milling are shown in Fig. 2. In early stages of ball milling, cold working predominates on soft particles of aluminum hence increasing their size but eventually brittle reinforcement particles of alumina and carbon nanotubes mix with aluminum increasing its brittleness, and

Fig. 1 Schematics diagram of cold spray process

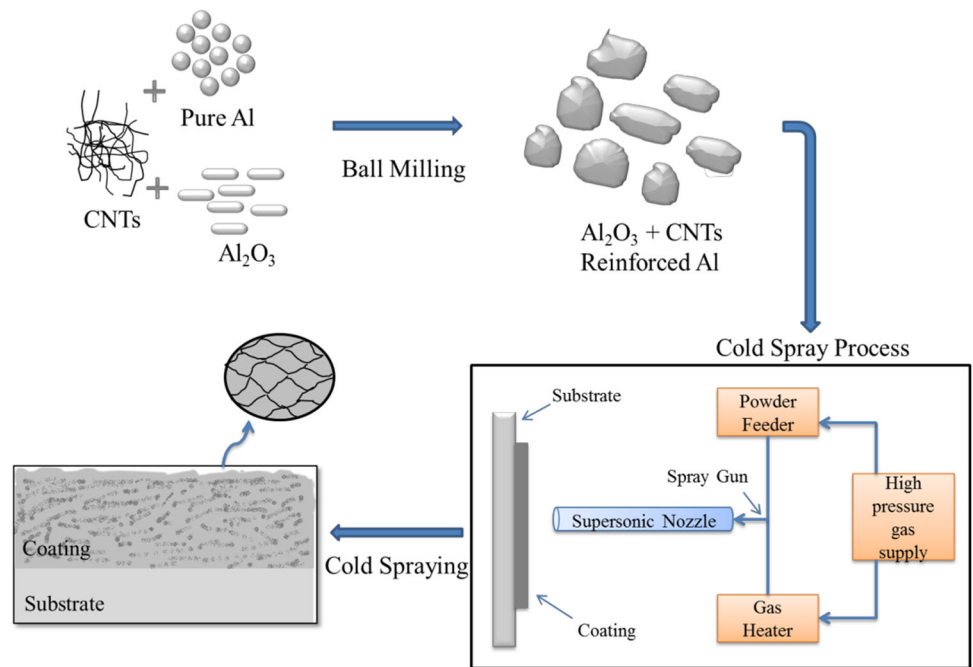
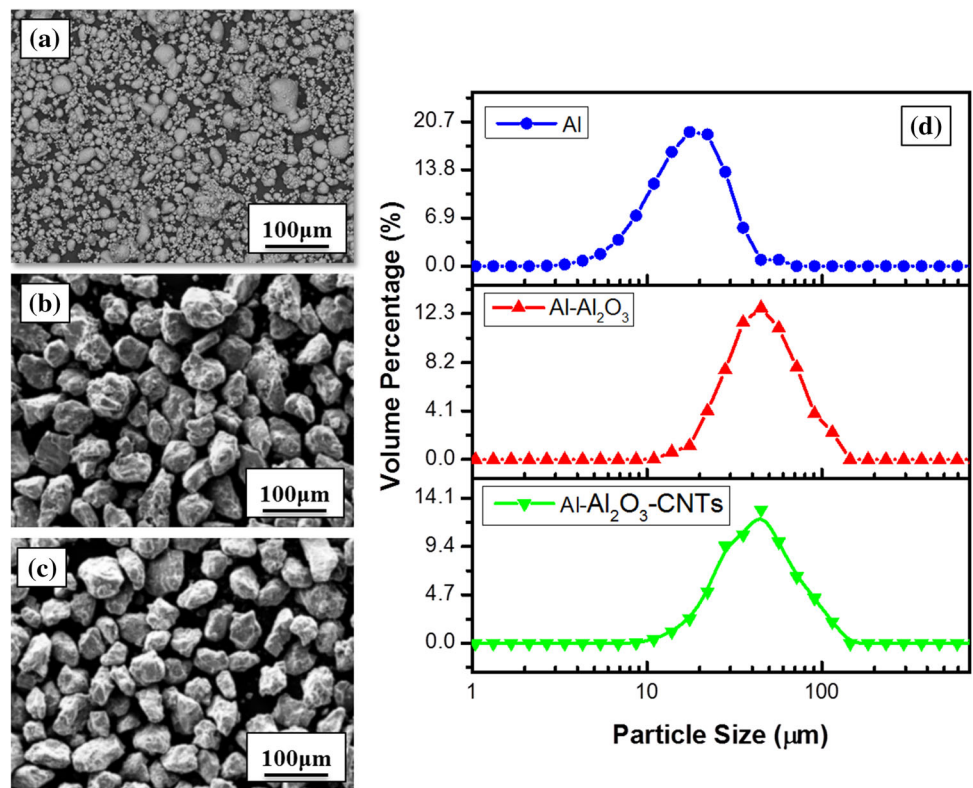


Fig. 2 Scanning electron micrographs of feedstock powders (a) Pure Al (b) Al + Al₂O₃ (c) Al + Al₂O₃ + CNTs after ball milling. (d) Particle size analysis of feed stock powders



consequently the fracture rate. It is evident from Fig. 2(b, c) that particles size of composite powders after ball milling increased and particles became less spherical due to the opposing effects of the two factors of cold work and fracturing of particles. Cold working results in particle size increment while fracturing of particles results in

morphologic changes (Ref 27). Figure 2(d) depicts the particle size analyses of samples, which affirms that the size of particles increases after ball milling.

XRD pattern of Pure Al, Al + Al₂O₃ and Al + Al₂O₃ + CNTs is shown in Fig. 3. XRD pattern of Pure Al revealed that all the diffraction peaks from Al matrix are

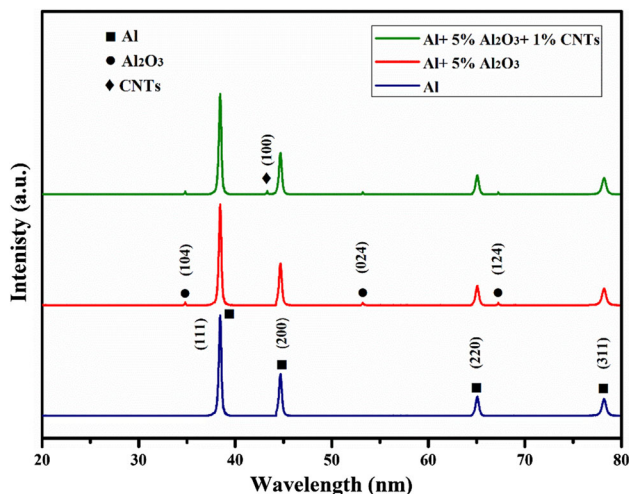


Fig. 3 X-ray diffraction pattern of feedstock powders

present belonging to the FCC crystal structure. Corresponding diffraction peaks are labeled clearly and are in precise match with literature reported previously (Ref 28, 29). The XRD pattern of Al_2O_3 and CNTs particle reinforced aluminum reflected that there is no peak shift due to mechanical ball milling. All the expected diffraction peaks from Al_2O_3 and CNTs were not observed in the corresponding XRD pattern. The only peaks present for Al_2O_3 were (104), (024) and (124) appearing at $2\theta = 34^\circ$, 53° and 67° while only one peak (100) for CNTs is observed at $2\theta = 43^\circ$. Also peaks from Al_2O_3 to CNTs have low intensity as compared to Aluminum peaks. This was attributed to the fact that reinforcing particles have fine size as well as low volume fraction in the powder mix. The crystallographic and microstructural observation shows the uniform distribution of reinforcing particles and indicated that no extra phase was present after ball milling.

Figure 4(a) depicts the FESEM micrograph of the polished cross section of the pure aluminum coatings. The images showed that the coating is dense and few pores are present. Figure 4(b) shows a magnified image of the same cross section and it revealed that few micropores are present. The Al- Al_2O_3 and Al- Al_2O_3 -CNTs coatings showed much denser structure with fewer pores, cracks and visible gaps as shown in Fig. 4(c, e). For further investigation, magnified images obtained by FESEM of Al- Al_2O_3 and Al- Al_2O_3 -CNTs coatings were taken and are presented in Fig. 4(d, f). Very few micropores are present, and the microstructure is dense. Ceramic particles trapped in the soft metal matrix break apart into tiny fragments through particle impacts. Coatings produced by the Al powder reinforced with CNTs and Al_2O_3 particles are reported to have very few micropores as compared to the pure Al coatings (Ref 19). It could be attributed to the low density of pure Al and thus a decreasing kinetic energy. The larger

density of the Al + Al_2O_3 than the pure Al enhances the kinetic impacting process and thus denser coatings during the deposition process. The high kinetic energy of the particles leads to the formation of dense coatings due to the deformation of the particles and peening of previous layer. Increased densification of the coatings with the addition of CNTs is possible as a result of the removal of surface oxide layers on the Al powders and eventuated in enhanced particles deformation during deposition process. FESEM micrographs reveal that crater-like formation is present at the top of cold-sprayed coatings owing to the tamping action of accelerated particles of feedstock powders (Table 1).

Figure 5 shows the micro-Vickers hardness profile of coatings as function of distance from substrate. Nonuniform distribution of particles resulted in wide dispersion of microhardness values. The microhardness of Al- Al_2O_3 and Al- Al_2O_3 -CNTs coatings revealed higher hardness values than pure Al coatings owing to the fact that hardness of cold-sprayed coatings mainly depends upon two factors which are porosity in coatings and work hardening degree of deposited particles (Ref 30). Al- Al_2O_3 -CNTs have maximum microhardness value because CNTs with better mechanical properties share the load applied on the matrix hence improving the mechanical properties of matrix. The highest microhardness values achieved by pure Al, Al- Al_2O_3 and Al- Al_2O_3 -CNTs coatings were (87.11 ± 2.12) , (89.21 ± 1.41) and (91.11 ± 1.71) HV, respectively. Also, microhardness profile reveals that the hardness near coating/substrate interface is higher than inside the substrate due to cold working from high-velocity interacting particles (Ref 31).

Corrosion Resistance Behavior

Open circuit potential (OCP) test was performed to evaluate the corrosion resistance performance of coatings in aqueous solution. Higher OCP values reflect better corrosion resistance of coatings (Ref 32), while the stable OCP curve indicates stability of formed film (Ref 33). The OCP evaluation of pure Al, Al- Al_2O_3 and Al- Al_2O_3 -CNTs coatings in 3.5% NaCl aqueous solution is shown in Fig. 6(a). OCP of substrate is also monitored in order to compare it with the coatings and the results are presented. The value of OCP for the substrate remained constant and after 1 h of immersion its potential was stabilized at $\sim (-1.5 \text{ V})$. The OCP curve of pure Al coating was steady and it showed higher potential value (-1.16 V) as compared to that of substrate. The OCP curve of the Al- Al_2O_3 coating started at a relatively lower value (-1.04 V) and then increased to and stabilized to (-1.00 V) : this is primarily due to passive film formation on the surface of the coating (Ref 34). The OCP curve of Al- Al_2O_3 -CNTs has a

Fig. 4 Cross-section images of pure Al coating at (a) lower and (b) higher magnification, cross-section images of Al-Al₂O₃ coating at (c) lower and (d) higher magnification, cross-section images of Al-Al₂O₃-CNTs coating at (e) lower and (f) higher magnification

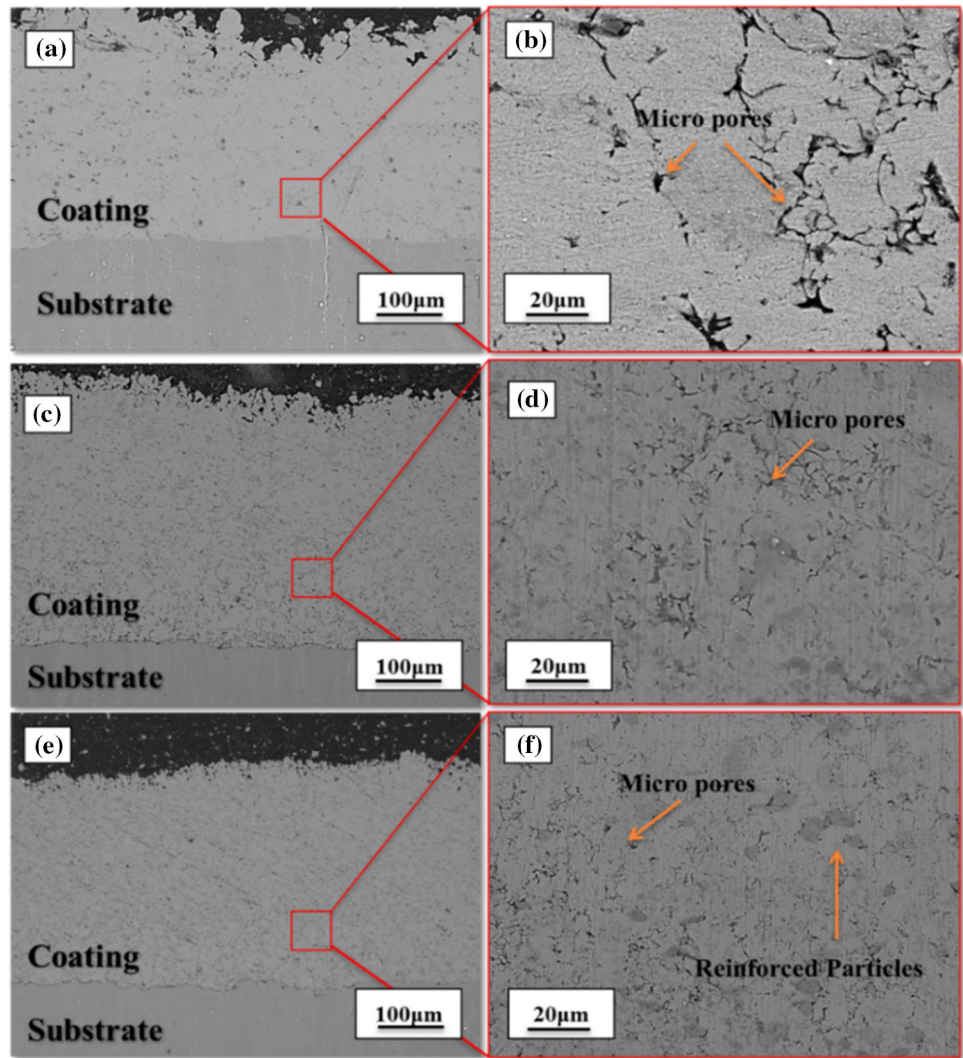


Table 1 Parameters of ball milling used for synthesis of feedstock powders

Parameters	Speed, rpm	Run-time, min	Rest-time, min	Total time, min	Steric acid	Ball size, mm	Powder feeder rate, g/min
Setting	180	1	1	480	0.25%	10	25

steady value around (− 0.92 V) and it is highest compared to the other samples. The metallic matrix coatings have higher electrode potential values as compared to Mg substrate and pure Al coating this depends upon intrinsic properties, decreased interparticle porosity and high density of the coatings. In this study, composite coatings with denser structure showed higher electrode potential behavior and hence have better corrosion resistance. Potentiodynamic polarization (PDP) test was also done to evaluate the corrosion resistance of coatings as well as that of substrate for comparison. Figure 6(b) shows the potentiodynamic polarization (PDP) curves. It is obvious from the

figure that coatings showed nobler corrosion potential (E_{corr}) and current density (I_{corr}) values as compared to the substrate. The corrosion potential of pure Al, Al-Al₂O₃ and Al-Al₂O₃-CNTs coatings was observed to be (− 1.17 ± 0.12 V), (− 1.03 ± 0.06 V) and (− 0.93 ± 0.04 V), respectively, which was higher than corrosion potential of the substrate (− 1.47 ± 0.14 V). The substrate also showed higher current density I_{corr} value (26.57 μA/cm²) while the I_{corr} values of pure Al, Al-Al₂O₃ and Al-Al₂O₃-CNTs coatings were (5.67 μA/cm²), (2.45 μA/cm²) and (0.87 μA/cm²), respectively. Lower current density value and higher corrosion potential reflect improved

corrosion resistance (Ref 35). Also Al-Al₂O₃ and Al-Al₂O₃-CNTs coatings show lesser oscillations and reduced electrochemical noise which depicts the reduction in pitting (Ref 36). This is mainly associated with denser microstructure and less microporosity in these coatings as evident from Fig. 4. The Tafel fitting results are listed in Table 2: it was found that the corrosion potential (E_{corr}) value of the samples increased significantly under the protection of the coating.

To further investigate the corrosion properties of Mg substrate, pure Al, Al-Al₂O₃ and Al-Al₂O₃-CNTs coatings electrochemical impedance spectroscopy (EIS) was done in 3.5% NaCl solution and results are presented in Fig. 7 with their equivalent corresponding circuits. The Nyquist plot of EIS has shown the basic characteristic for Mg substrate. The impedance diameter of the substrate was smaller as

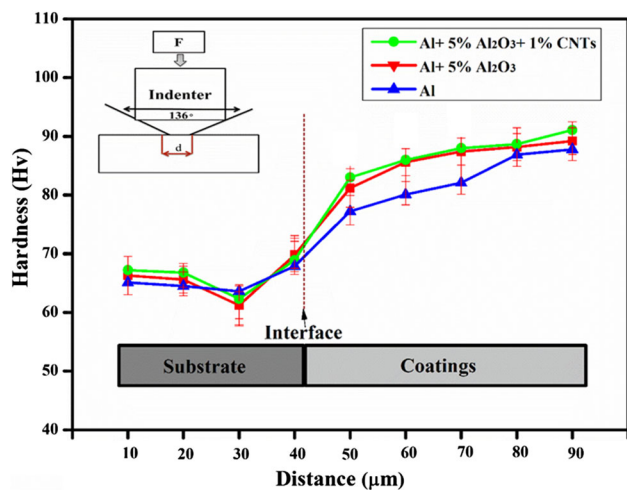
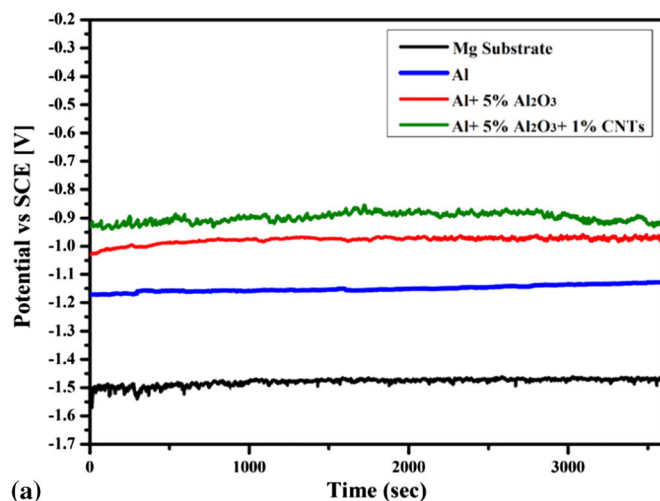


Fig. 5 Hardness profile of pure Al, Al-Al₂O₃, Al-Al₂O₃-CNTs coatings as function of distance from substrate



compared to the coatings. Also, the substrate showed a capacitive loop at high frequency and inductive loop at lower frequency. The inductive loop indicates that pitting corrosion and oxide film dissolution occur on the substrate surface. In addition, it also accounts for the high chemical reactivity of the substrate during the test. The inductive loop in Nyquist plots indicates the electrochemical dissolution of passivation film at the outer layer in general. The capacitive loop shows electron transfer resistance during electrochemical process while the inductive loop represents the electrochemical dissolution of passive film. EIS plots of pure Al coating have relatively straight lines, this shows that a mass transfer stage is involved in the corrosion process of these samples. It is found that there are two capacitor loops in case of Al₂O₃ and CNTs reinforced coatings at intermediate and low frequency, respectively. The capacitive loop at low frequency reflects the interface charge transfer behavior of a corroded system. The diameter of low frequency loop reflects the difficulty of interface charge transfer between the coating and the test solution. The intermediate frequency loop represents the properties of the oxide film formed on the substrate surface. Since the loose and porous oxide film on the surface of the

Table 2 Potentiodynamic polarization and Tafel extrapolation results of Mg substrate and pure Al, Al-Al₂O₃, Al-Al₂O₃ + CNTs coatings

Coatings	E_{corr} (V vs SCE)	I_{corr} ($\mu\text{A}/\text{cm}^2$)
Mg substrate	-1.47 ± 0.14	26.57 ± 2.21
Pure Al coating	-1.17 ± 0.12	5.67 ± 0.84
Al-Al ₂ O ₃	-1.03 ± 0.06	2.45 ± 1.21
Al-Al ₂ O ₃ -CNTs	-0.93 ± 0.04	0.87 ± 0.45

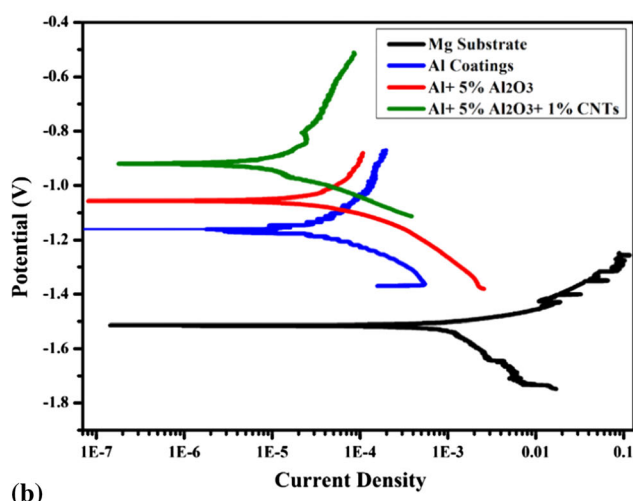


Fig. 6 (a) OCP curves as a function of time (b) potentiodynamic polarization curves of Mg substrate and pure Al, Al-Al₂O₃, Al-Al₂O₃ + CNTs coatings

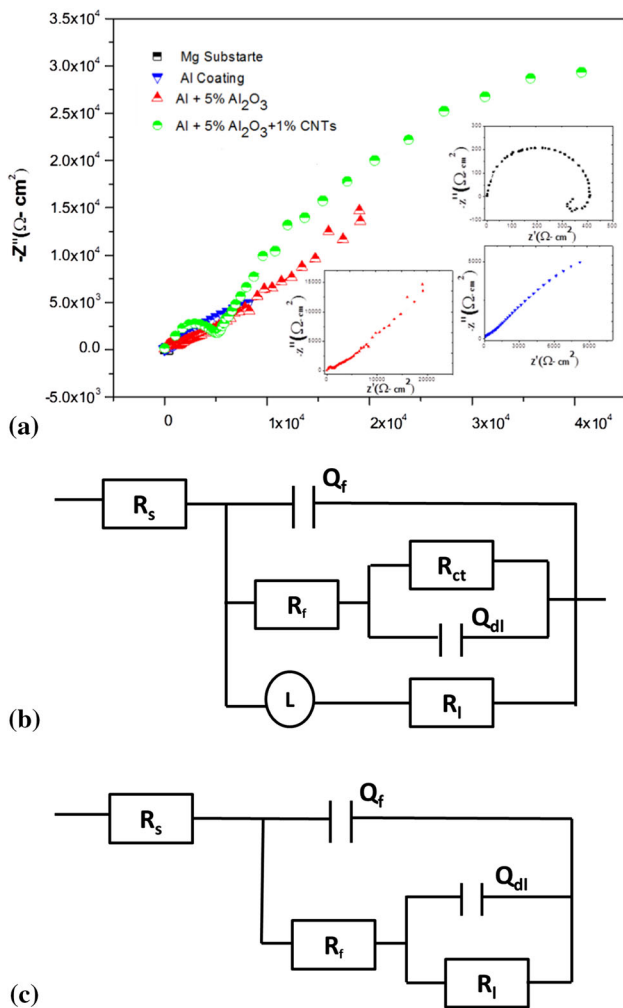


Fig. 7 (a) Electrochemical impedance spectroscopy Nyquist plots of Mg substrate and pure Al, Al-Al₂O₃, Al-Al₂O₃ + CNTs coatings (b) Equivalent circuits of EIS results

Mg alloys can hardly block the corrosive medium from reaching the substrate, so the capacitive loop at the intermediate frequency is not particularly obvious (Ref 37). Equivalent circuits models shown in Fig. 7(b) are used to fit the experimental spectra of EIS and for simulation of interfacial electrochemical process occurring at metal/electrolyte interface. The EIS spectrum of LA43M substrate can be fitted by using $R_s (Q_f(R_f(Q_{dl} R_{ct}))(R_l L))$ model, as shown in Fig. 7(b). R_f is the resistance of the oxide film on the surface of the LA43M alloy, and the value of R_f is only $561.2 \Omega \text{ cm}^2$. Q_f is the capacitive behavior of the passive film. R_s represents the solution resistance, R_{ct} is the charge transfer resistance, and Q_{dl} refer to the electrical double layer capacitive behavior on the substrate interface (Ref 38). The EIS spectrum of the samples with coating can be fitted with equivalent circuit model of $R_s (Q_f(R_f(Q_{dl} R_{ct})))$ in Fig. 7(b). R_{ct} is an important parameter in measurement of corrosion

resistance by EIS as it represents the active protection delivered by the coatings. The value of R_{ct} for the Al-Al₂O₃-CNTs coating is $(7.57 \times 10^3 \pm 0.29 \times 10^3 \Omega \text{ cm}^2)$ and for the Al-Al₂O₃, pure Al and the substrate the values are $(6.23 \times 10^3 \pm 4.84 \times 10^2 \Omega \text{ cm}^2)$ $(1.35 \times 10^3 \pm 2.61 \times 10^2 \Omega \text{ cm}^2)$ and $(7.12 \times 10^2 \pm 0.16 \times 10^2 \Omega \text{ cm}^2)$, respectively. As the Al-Al₂O₃-CNTs coating showed a R_{ct} value that is almost four times in magnitude than that of the substrate and almost double to that of the pure Al coatings we can deduct that the impedance response is practically given by the coating with extremely low contribution of the substrate, indicating that the coating is protecting the substrate (Ref 39). So Al matrix coatings not only improved the corrosion resistance of substrate but also have better corrosion resistance properties than the pure Al coating (Table 3).

Figure 8(a) shows the comparison among the weight losses of Mg substrate, pure Al, Al-Al₂O₃ and Al-Al₂O₃-CNTs coatings in the immersion test in 3.5% NaCl solution as function of time. Due to severe corrosion losses, the Mg substrate shows almost a linear relationship between immersion time and weight loss. Real images of substrate surface before and after immersion test display a clear difference as the surface corroded sternly due to immersion in the NaCl solution and pits appeared on the surface. After 1000 h of immersion, the substrate almost lost one third of its total weight. Similar results are presented by Jahed et al. (Ref 40) in their research. The pure Al coating showed little weight loss at the beginning but after 100 h of immersion there was no loss, which showed that corrosion products were protective and further stopped the corrosion of the substrate as the coating was undergoing slow corrosion. On the other hand, Al-Al₂O₃ and Al-Al₂O₃-CNTs coatings showed almost no weight loss even after 1000 h of immersion which illustrates the fact that they have very good corrosion resistance. Visual representation of Pure Al, Al-Al₂O₃ and Al-Al₂O₃-CNTs coatings showed no pits or localized corrosion on the surface. It is worth mentioning here that none coating spall from the Mg substrate was observed after the immersion test.

Wear Behavior

Figure 9(a) shows the coefficient of friction (COF) of coatings as well as substrate as function of sliding distance while Fig. 9(b) shows the average COF of the specimens. Figure 9(a) shows the coefficient of friction (COF) of the coatings as well as COF of the Mg substrate as a function of the sliding distance while Fig. 9(b) indicates the average COF of the specimens tested. Al coatings have demonstrated higher COF values and different forms of wear relative to Al-Al₂O₃ and Al-Al₂O₃-CNT coatings. The Mg substrate displayed the maximum mean COF value

Table 3 Quantitative information received by modeling of EIS equivalent circuits

Coatings	R_1	L	R_s	Q_f	R_f	R_{ct}	Q_{dl}	x^2 ($\times 10^{-2}$)
Mg substrate	$452 \pm 28 \Omega \text{ cm}^2$	$880 \pm 42 \text{ H cm}^2$	$9.45 \pm 1.28 \Omega \text{ cm}^2$	$1.03 \times 10^{-5} \pm 3.21 \times 10^{-6} \text{ S s}^0/\text{cm}^2$	$5.61 \times 10^2 \pm 0.28 \times 10^2 \Omega \text{ cm}^2$	$7.12 \times 10^2 \pm 0.16 \times 10^2 \Omega \text{ cm}^2$	$1.24 \times 10^{-5} \pm 2.73 \times 10^{-6} \text{ S s}^0/\text{cm}^2$	4.6 ± 0.4
Pure Al coating	$8.67 \pm 1.61 \Omega \text{ cm}^2$	$9.02 \times 10^{-5} \pm 1.63 \times 10^{-6} \text{ S s}^0/\text{cm}^2$	$8.57 \times 10^3 \pm 1.51 \times 10^2 \Omega \text{ cm}^2$	$1.35 \times 10^3 \pm 2.61 \times 10^2 \Omega \text{ cm}^2$	$4.08 \times 10^{-5} \pm 1.67 \times 10^{-6} \text{ S s}^0/\text{cm}^2$	3.4 ± 0.2
Al-Al ₂ O ₃	$7.78 \pm 1.34 \Omega \text{ cm}^2$	$4.47 \times 10^{-6} \pm 2.26 \times 10^{-7} \text{ S s}^0/\text{cm}^2$	$4.09 \times 10^4 \pm 3.42 \times 10^2 \Omega \text{ cm}^2$	$6.23 \times 10^3 \pm 4.84 \times 10^2 \Omega \text{ cm}^2$	$2.43 \times 10^{-6} \pm 9.11 \times 10^{-7} \text{ S s}^0/\text{cm}^2$	2.2 ± 0.7
Al-Al ₂ O ₃ -CNTs	$5.89 \pm 0.89 \Omega \text{ cm}^2$	$2.01 \times 10^{-7} \pm 0.29 \times 10^{-7} \text{ S s}^0/\text{cm}^2$	$2.05 \times 10^5 \pm 2.17 \times 10^3 \Omega \text{ cm}^2$	$7.57 \times 10^4 \pm 0.29 \times 10^3 \Omega \text{ cm}^2$	$7.57 \times 10^{-6} \pm 4.87 \times 10^{-7} \text{ S s}^0/\text{cm}^2$	3.1 ± 0.3

(0.71 ± 0.02) and unstable friction curve. It can be seen that the COF curve of Mg substrate was not steady at all and it shows a certain increase and decrease behavior. This is due to the release of wear debris by the uncoated sample during testing, wear debris increases the contact area. The fluctuation of COF can be attributed to excessive subsurface fracturing and delamination as well. On the other side, the COF curve of each coating stayed nearly unchanged and the pure Al, Al-Al₂O₃ and Al-Al₂O₃-CNT coatings displayed average COF values of about (0.51 ± 0.02), (0.46 ± 0.02) and (0.39 ± 0.01), respectively. The Al-Al₂O₃-CNTs have the lowest COF value, which is attributed to the fact that it has a denser microstructure and the maximum Vickers microhardness resulting in a decrease in the region of contact hence reduced force of friction. The pure Al COF curve showed a steady value at first but after some time it suddenly showed a peak in COF value and then again it became stable. This sudden peak in COF value was due to unsteady abrasion. Reinforcing particles also decreased the COF of the coatings as they share the strain on the Al matrix and contribute to the densification of the microstructure of the coatings (Ref 41). It can be concluded from the results that the reinforcement of hard particles has significantly decreased the COF and the Al-Al₂O₃-CNTs coating has the lowest COF value as compared to the other coatings.

Figure 10(a) shows the wear rate of coatings and substrate. Lower wear rate represents better wear resistance of the specimen (Ref 42). It is clear from the figure that the wear rate of the Mg substrate is comparatively higher as compared to Al and Al matrix composite coatings. Wear rates of Mg substrate, pure Al, Al-Al₂O₃ and Al-Al₂O₃-CNTs coatings are ($4.35 \times 10^{-2} \pm 9.11 \times 10^{-5} \text{ mm}^3/\text{m}$), ($6.78 \times 10^{-3} \pm 3.13 \times 10^{-4} \text{ mm}^3/\text{m}$), ($1.21 \times 10^{-3} \pm 6.22 \times 10^{-5} \text{ mm}^3/\text{m}$) and ($4.43 \times 10^{-4} \pm 3.41 \times 10^{-5} \text{ mm}^3/\text{m}$), respectively. Reinforcing particles decreased the wear rate of the coatings because they share the load on Al matrix and also result in densification of the microstructure of the coatings. Also the wear rate measurements support the COF data as they show the same tribological behavior. Figure 10(b) shows the mass of samples after wear testing, it can be seen that the Mg substrate lost around three times more mass as compared to the coatings. The worn surface of the Mg substrate shown in Fig. 10(c) depicts a number of grooves present in the direction parallel to sliding which is an example of typical abrasive wear. Some debris particles are also seen on the worn surface. Figure 10(d, e) presents the worn surfaces of the Al-Al₂O₃ and Al-Al₂O₃-CNTs coatings and it can be seen that they show adhesive delamination of the surface layer. Also during the wear test, some microcracks initiated though the surface particle are bounded strongly. Propagation of cracks results in

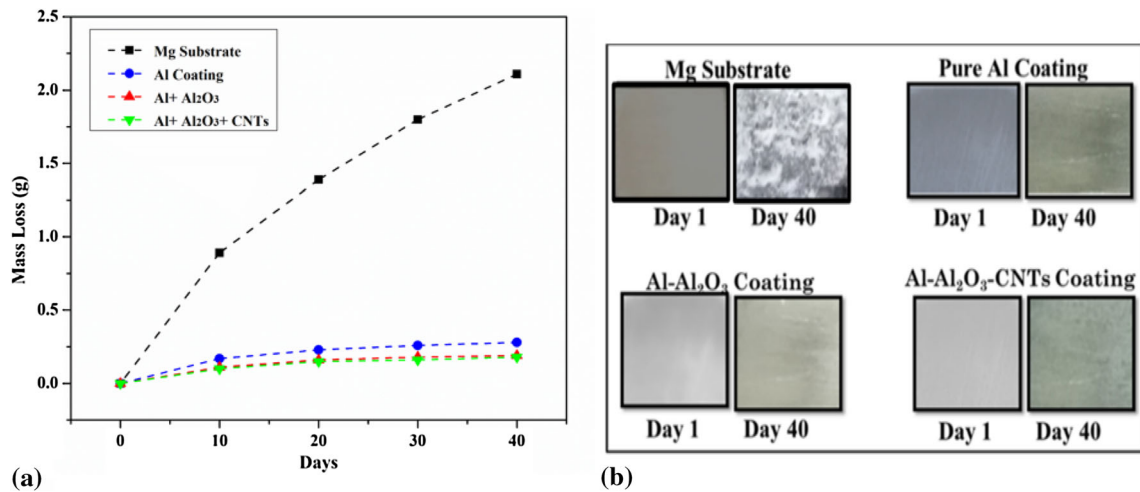


Fig. 8 (a) Long-term immersion test results of Mg substrate and pure Al, Al-Al₂O₃, Al-Al₂O₃ + CNTs coatings in 3.5% NaCl Solution (b) Visual representation of samples after test

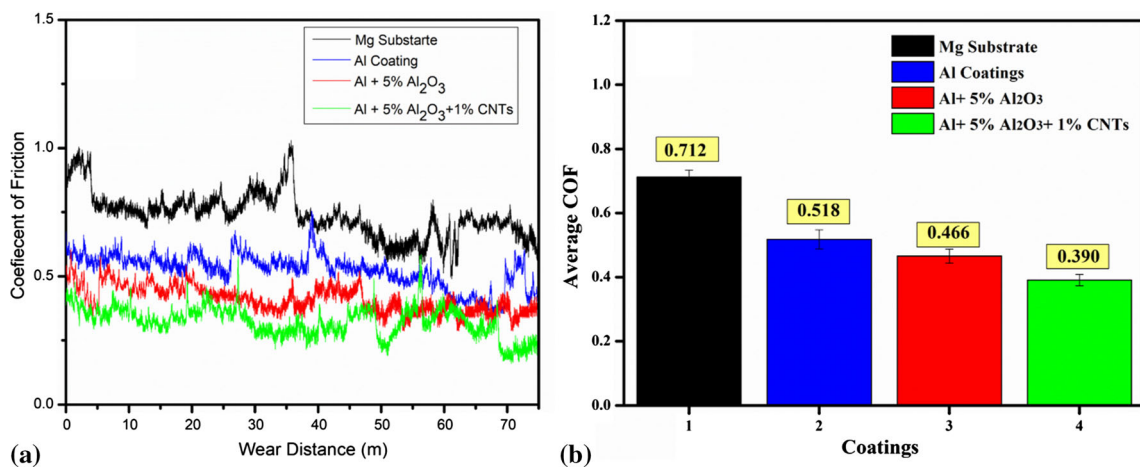


Fig. 9 (a) COF of Mg substrate and pure Al, Al-Al₂O₃, Al-Al₂O₃ + CNTs coatings. (b) Average COF after wear test

delamination and deformation due to continuous plowing process (Ref 43, 44).

Conclusion

In this research work, the tribological behavior and corrosion resistance of pure Al, Al-Al₂O₃ and Al-Al₂O₃-CNTs coatings were investigated. The corrosion and tribological behavior of cold-sprayed coatings mainly depends upon the microstructure developed during spraying. We observed that the reinforcement of hard particles, i.e., Al₂O₃ and CNTs in MMC coatings resulted in densification of coating microstructure with fewer visible micropores. Thus, the

corrosion resistance of Mg substrate was improved. Electrochemical results illustrated that Al-Al₂O₃ and Al-Al₂O₃-CNTs coatings have better anticorrosion resistance properties than pure Al coating and Mg substrate and Al-Al₂O₃-CNT coating processed superlative corrosion resistance. The corrosion potential of the Al-Al₂O₃-CNTs composite coating has been improved and the corrosion current density is 0.87 μA/cm², which is much lower than the LA43M substrate. Reinforcement of Al₂O₃ and CNTs in Al not only enhanced the electrochemical properties of coating but also resulted in better wear resistance. The tribological study confirmed that Al-Al₂O₃-CNT coating mentioned in this work has better wear properties than other samples.

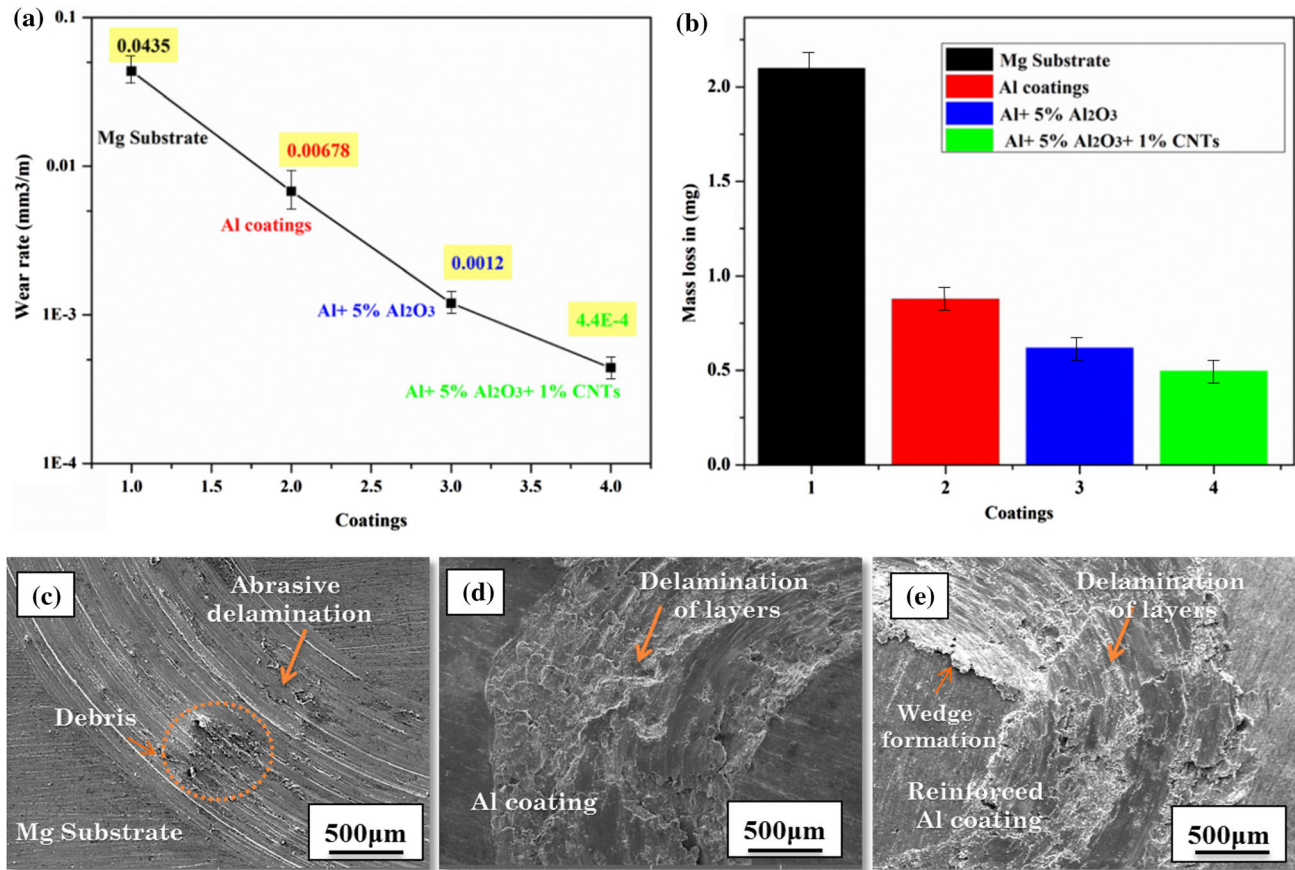


Fig. 10 (a) Wear rate and wear volume profile of Mg substrate and pure Al, Al-Al₂O₃, Al-Al₂O₃ + CNTs coatings. (b) Average mass loss after wear test (c) FESEM micrographs of worn surface of Mg Substrate and pure Al, Al-Al₂O₃, Al-Al₂O₃ + CNTs coatings

Acknowledgment This work was supported by the National Key Research and Development Program of China (Basic Research Project, Grant No. 2017YFB0306100) and the National Key Research and Development Program of China (China-USA Intergovernmental Cooperation Project, Grant No. 2017YFE0105900).

References

1. G. Manoj and M. Ling, Magnesium, Magnesium Alloys and Magnesium Composites, *Mater. Sci. Appl.*, 2010, **09**, p 1021-1035
2. C. Xianhua, G. Yuxiao, and P. Fusheng, Research Progress in Magnesium Alloys as Functional Materials, *Rare Met. Mater. Eng.*, 2016, **45**, p 2269-2274
3. Y. Kojima, T. Aizawa, and S. Kamado, Magnesium Alloys Development Towards the 21st Century, *Mater. Sci. Forum*, 2010, **350**, p 19-30
4. Y. Sun, R. Wang, C. Peng, Y. Feng, and M. Yang, Corrosion Behavior and Surface Treatment of Superlight Mg-Li Alloys, *Trans. Nonferrous Met. Soc. China*, 2017, **27**, p 1455-1475
5. J. Gray and B. Luan, Protective Coatings on Magnesium and Its Alloys—A Critical Review, *J. Alloys. Compd.*, 2003, **336**, p 87-113
6. M. Parco, M.C. Merin, M. Mohedano, P. Casajús, A.E. Coy, and R. Arrabal, Investigation of HVOF Spraying on Magnesium Alloys, *Surf. Coat. Technol.*, 2001, **201**, p 3269-3274
7. H. Pokhmurska, B. Wielage, and T. Lampke, Post-treatment of Thermal Spray Coatings on Magnesium, *Surf. Coat. Technol.*, 2009, **202**, p 4515-4524
8. Z. Wei, L. Liu, and J. Ding, Al Arc Spray Coating on AZ31 Mg Alloy and Its Corrosion Behavior, *Mater. Sci. Forum*, 2005, **102**, p 685-688
9. H. Zhou, C. Li, G. Ji, S. Fu, H. Yang, X. Luo, G. Yang, and C. Li, Local Microstructure Inhomogeneity and Gas Temperature Effect in In-Situ Shot-Peening Assisted Cold-Sprayed Ti-6Al-4 V Coating, *J. Alloys Compd.*, 2018, **766**, p 694-704
10. S.-L. Fu, C.-X. Li, Y.-K. Wei, X.-T. Luo, G.-J. Yang, C.-J. Li, and J.-L. Li, Novel Method of Aluminum to Copper Bonding by Cold Spray, *J. Therm. Spray Technol.*, 2018, **27**, p 624-640
11. E. Irissou, J.G. Legoux, B. Arsenault, and C. Moreau, Investigation of Al-Al₂O₃ Cold Spray Coating Formation and Properties, *J. Therm. Spray Technol.*, 2007, **16**, p 661-667
12. C. Borchers, F. Gärtner, and T. Stoltenhoff, Microstructural Bonding Features of Cold Sprayed Face Centered Cubic Metals, *J. Appl. Phys.*, 2003, **96**, p 4288-4292
13. A. Zuniga, B. Jodoin, and E.J. Lavernia, Cold Gas Dynamic Spraying of a High Temperature Al Alloy, *Surf. Coat. Technol.*, 2006, **201**, p 2109-2116
14. K. Kang and S. Bong, Tungsten/Copper Composite Deposits Produced by a Cold Spray, *Scripta Mater.*, 2009, **49**, p 1169-1174
15. Y.-K. Wei, X.-T. Luo, Y. Ge, X. Chu, G.-S. Huang, and C.-J. Li, Deposition of Fully Dense Al-Based Coatings via In-Situ Microforging Assisted Cold Spray for Excellent Corrosion Protection

- of AZ31B Magnesium Alloy, *J. Alloys Compd.*, 2019, **806**, p 1116-1126
16. J. Hoddera, H. Izadia, A. McDonald, and P. Gerlichc, Fabrication of Aluminum–Alumina Metal Matrix Composites via Cold Gas Dynamic Spraying at Low Pressure Followed by Friction Stir Processing, *Mater. Sci. Eng., A*, 2012, **556**, p 114-121
 17. S. Ngai, T. Ngai, F. Vogel, W. Story, G.B. Thompson, and L.N. Brewer, Saltwater Corrosion Behavior of Cold Sprayed AA7075 Aluminum Alloy Coatings, *Corros. Sci.*, 2018, **130**, p 231-240
 18. X.C. Zhang, B.S. Xu, Y.X. Wu, F.Z. Xuan, and S.T. Tu, Porosity, Mechanical Properties, Residual Stresses of Supersonic Plasma-Sprayed Ni-Based Alloy Coatings Prepared at Different Powder Feed Rates, *Appl. Surf. Sci.*, 2008, **254**, p 3879-3889
 19. D. Poirier, J. Legoux, and L. Drew, Consolidation of Al₂O₃/Al Nanocomposite Powder by Cold Spray, *J. Therm. Spray Technol.*, 2012, **20**, p 275-284
 20. K. Spencer, M. Fabijanic, and X. Zhang, The Use of Al-Al₂O₃ Cold Spray Coatings to Improve the Surface Properties of Magnesium Alloys, *Surf. Coat. Technol.*, 2009, **204**, p 336-344
 21. H. Kim, C. Lee, and S. Hwang, Superhard Nano WC-12%Co Coating by Cold Spray Deposition, *Mater. Sci. Eng., A*, 2005, **391**, p 243-248
 22. A. Kin and D. Hui, The Revolutionary Creation of New Advanced Materials—Carbon Nanotube Composites, *Compos. B Eng.*, 2002, **33**, p 263-277
 23. A. Aborkin, K. Khorkov, E. Prusov, A. Obedkov, K. Kremlev, I. Perezhogin, and M. Alymov, Effect of Increasing the Strength of Aluminum Matrix Nanocomposites Reinforced with Microadditions of Multiwalled Carbon Nanotubes Coated with TiC Nanoparticles, *Nanomaterials*, 2019, **9**, p 1596-1599
 24. J. Lou, A. Cheng, P. Zhao, R. Misra, and H. Feng, The Significant Impact of Carbon Nanotubes on the Electrochemical Reactivity of Mg-Bearing Metallic Glasses with High Compressive Strength, *Materials*, 2019, **12**, p 2989-2997
 25. R. Wong and D. Knitter, Manufacturing of Ceramic Microcomponents by a Rapid Prototyping Process Chain, *Adv. Eng. Mater.*, 2001, **23**, p 23-29
 26. I. Ozdemir, S. Ahrens, and S. Mucklich, Nanocrystalline Al-Al₂O₃p and SiCp Composites Produced by High-Energy Ball Milling, *J. Mater. Process. Technol.*, 2008, **205**, p 111-118
 27. B. Prabhua, C. Suryanarayan, L. Anab, and R. Vaidyanathan, Synthesis and Characterization of High Volume Fraction Al-Al₂O₃ Nanocomposite Powders by High-Energy Milling, *Mater. Sci. Eng., A*, 2006, **425**, p 192-200
 28. Y. Lui and L. Wang, XRD and SEM Analysis Near the Diffusion Bonding Interface of Mg/Al Dissimilar Materials, *Vacuum*, 2007, **52**, p 15-19
 29. G. Sun, J. Young, and J. Kirkpatrick, The Role of Al in C-S-H: NMR, XRD, and Compositional Results for Precipitated Samples, *Cem. Concr. Res.*, 2006, **36**, p 18-29
 30. Q. Jin, G. Tian, J. Li, Y. Zhao, and H. Yan, The Study on Corrosion Resistance of Superhydrophobic Magnesium Hydroxide Coating on AZ31B Magnesium Alloy, *Colloids Surf. A*, 2019, **577**, p 8-16
 31. G. Zhang, L. Wu, A. Tang, Y. Ma, G. Song, D. Zheng, B. Jiang, A. Atrens, and F. Pan, Active Corrosion Protection by a Smart Coating Based on a MgAl-Layered Double Hydroxide on a Cerium-Modified Plasma Electrolytic Oxidation Coating on Mg Alloy AZ31, *Corros. Sci.*, 2018, **139**, p 370-382
 32. M. Yin, A. Boiyuyt, and M. Sun, Self-Healing Plasma Electrolytic Oxidation Coatings Doped with Benzotriazole Loaded Halloysite Nanotubes on AM50 Magnesium Alloy, *Corros. Sci.*, 2016, **11**, p 753-769
 33. Y. Zhu, G. Yu, and B. Hu, Electrochemical Behaviors of the Magnesium Alloy Substrates in Various Pretreatment Solutions, *Appl. Surf. Sci.*, 2010, **256**, p 2988-2994
 34. S. Pyun and W. Lee, The Effect of Prior Cl⁻ Ion Incorporation into Native Oxide Film on Pure Aluminium in Neutral Chloride Solution on Pit Initiation, *Corros. Sci.*, 2001, **43**, p 353-363
 35. H. Hongwwi, Y. Li, and F. Wang, Improvement on the Corrosion Resistance of AZ91D Magnesium Alloy by Aluminum Diffusion Coating, *J. Mater. Sci. Technol.*, 2007, **24**, p 29-38
 36. Y. Tao, T. Xiong, and C. Sun, Microstructure and Corrosion Performance of a Cold Sprayed Aluminium Coating on AZ91D Magnesium Alloy, *Corros. Sci.*, 2010, **34**, p 3191-3197
 37. H. Bu, M. Yandozi, C. Lu, and B. Jodoin, Effect of Heat Treatment on the Intermetallic Layer of Cold Sprayed Aluminum Coatings on Magnesium Alloy, *Surf. Coat. Technol.*, 2011, **205**, p 4665-4671
 38. Y. Tao, T. Xiong, and C. Sun, Effect of α -Al₂O₃ on the Properties of Cold Sprayed Al/ α -Al₂O₃ Composite Coatings on AZ91D Magnesium Alloy, *Appl. Surf. Sci.*, 2009, **256**, p 261-266
 39. J. Colin and A. Kuhn, Electrochemical and Density Functional Theory Study of Bis(cyclopentadienyl) Mono(β -diketonato) Titanium(IV) Cationic Complexes, *Electrochim. Acta*, 2010, **56**, p 257-264
 40. M. Diab, X. Pang, and H. Jahed, The Effect of Pure Aluminum Cold Spray Coating on Corrosion and Corrosion Fatigue of Magnesium (3% Al-1% Zn) Extrusion, *Surf. Coat. Technol.*, 2017, **309**, p 423-435
 41. P. Long, C. Zui, and C. Xu, Wear and Corrosion Resistance of Laser Cladding AISI, 304 Stainless Steel/Al₂O₃ Composite Coatings, *Surf. Coat. Technol.*, 2014, **252**, p 9-14
 42. S. Salven and S. Ramanathan, Dry Sliding Wear Behavior of As-Cast ZE41A Magnesium Alloy, *Mater. Des.*, 2010, **31**, p 1930-1936
 43. Q. Song, N. Shang, and X. Zhang, Wear Behaviour of AZ91D Magnesium Alloy with a Nanocrystalline Surface Layer, *Surf. Coat. Technol.*, 2008, **202**, p 2859-2864
 44. F. Silvaa, N. Cincab, and S. Dostab, Corrosion Behavior of WC-Co Coatings Deposited by Cold Gas Spray onto AA 7075-T6, *Corros. Sci.*, 2010, **108**, p 111-115

Publisher's Note Springer Nature remains neutral with regard to jurisdictional claims in published maps and institutional affiliations.